Non-volatile memory characteristics of a Ti/HfO_2/Pt synaptic device with a crossbar array structure

Osung Kwon and Sungjun Kim*
Division of Electronics and Electrical Engineering, Dongguk University, Seoul 04620, South Korea
Nikolay Agudov[a], Alexey Krichigin[a], Alexey Mikhaylov[a], Roberto Grimaudo[b], Davide Valenti[b], Bernardo Spagnolo[a,b]
[a]Stochastic Multstable Systems Laboratory, Lobachevsky University, Nizhny Novgorod 603022, Russia
[b]Dipartimento di Fisica e Chimica “Emilio Segrè”, Group of Interdisciplinary Theoretical Physics, Università degli Studi di Palermo and CNISM, Unità di Palermo, Viale delle Scienze, Edificio 18, I-90128 Palermo, Italy
*Corresponding author: sungjun@dongguk.edu

ABSTRACT
The resistive switching and synaptic behavior of a fabricated Ti/HfO_2/Pt crossbar array device are investigated. The results demonstrated that TiO_x layers are created by the movement of oxygen ions during the positive SET process, thereby improving the endurance and multilevel switching behavior of the device. The random properties of SET process were described with the help of stochastic model of memrisor based on the length of conductive filament. The analysis of the mean first passage time allows to estimate the parameters of the dielectric switching layer such as the activation energy of the diffusive defects, its variation under the influence of the driving voltage and the value of the working temperature. Furthermore, the conductive mechanism of the Ti/HfO_2/Pt device with temperature variations and Schottky emission fitting was studied. Furthermore, the potentiation, depression, and the spike-time dependent plasticity behavior of the Ti/HfO_2/Pt devices have been demonstrated by well-designed pulse inputs. The observed gradual change in conductance is suitable for a synaptic device in a neuromorphic system.

Introduction

The human brain, which contains more than 100 billion neurons and 100 trillion synapses, is efficient in solving complex problems while consuming very little energy [1]. Recently, new memory devices such as phase-change random access memory (PRAM), magnetoresistive RAM (MRAM), and resistance RAM (RRAM) have been created by imitating these efficient human brain structures, and have emerged as neuromorphic and neurohybrid devices [2–5]. Indeed, neuromorphic computing has emerged as a promising way towards the next generation of intelligent computing systems [6, 7]. The memristor, a new 2-terminal device with a number of attractive properties [8, 9], is considered an excellent emulator of biological synapses and neurons that are fundamental elements for brain inspired neuromorphic computing [10-17]. Indeed, the new memory and processing systems will revolutionize today's computer performance [18, 19].

In particular, RRAM, which is based on new materials such as metal oxides and organic compounds, is emerging as a promising nonvolatile memory candidate [2]. The electrically generated resistance switching phenomenon has been observed in oxides such as AlO_x, WO_x, HfO_x, ZrO_x, and TaO_x [20]. These materials have been observed to exhibit good endurance, low-power operation [21–25], fast switching speeds [23,24,26], and well-controlled multilevel conductivity [27–35].

In recent years, many studies have been actively conducted on the crossbar array structure as a good approach towards improving neuromorphic systems and resolving the physical scaling problems [1], [28–30]. In a crossbar array structure, each memory cell is positioned at the intersection of two perpendicular metal lines, and can be scaled down to a small size in nanometer units [36]. However, in this crossbar array structure, there is a sneak current path issue that causes read operation error and array size limitation [30,31]. A two-terminal memristor device with a crossbar array structure composed of these materials can mimic the

54 biological synaptic function. Furthermore, these memristors can simulate long-term
55 potentiation (LTP) and long-term depression (LTD) characteristics by application of a
56 repeated pulse voltage [37]. For instance, HfO_2 has been reported to produce many oxygen
57 vacancies and oxygen ions after the forming process [22,38]. When the metal-oxygen bond is
58 broken, oxygen vacancies are generated in the oxide layer. The generation and disruption of
59 conductive filaments produced by these oxygen vacancies are central to the switching process
60 of the HfO_2-based RRAM devices [22,39]. Furthermore, it is worthwhile to note that the
61 switching process in memristor devices is a stochastic process which characterize their
62 dynamics with interesting noise-induced phenomena as those observed in many
63 interdisciplinary physics models [40-49].

64 In the present study, a Ti/HfO_2/Pt device is first fabricated and verified using energy
65 dispersive X-ray spectroscopy (EDS), scanning electron microscopy (SEM), and transmission
66 electron microscopy (TEM). In addition, the current-voltage (I-V) curves with abrupt positive
67 SET and gradual negative RESET are characterized, and the stress effect of 10,000 pulses
68 upon resistive switching behaviors are investigated. In detail, the pulse voltage dependent
69 switching speed is studied in the SET process, and multilevel characteristics are achieved in
70 the RESET process. Since the variability is essential feature of memristors, the stochastic
71 properties of the SET process are investigated on the basis of a stochastic model [50,51]. The
72 conduction mechanisms of the SET and RESET processes are presented. Furthermore, the
73 synaptic properties of the Ti/HfO_2/Pt devices are emulated through spike-time-dependent
74 plasticity (STDP) measurements. Finally, the LTP and LTD characteristics of the Ti/HfO_2/Pt
75 devices are obtained using both identical pulse and incremental pulse schemes.

76

77

78 **Experimental setup**

79 A 100-nm thick Pt bottom electrode (BE) was deposited on a SiO_2/Si wafer using an e-beam
80 evaporator. The BE pattern was fabricated via photolithographic and lift-off processes. A 5-
81 nm thick HfO_2 switching layer was deposited via atomic layer deposition (ALD) with tetrakis
82 (dimethylamino)hafnium (TDMAHF) as the Hf source, and O_3 as the oxygen source. One
83 cycle of the ALD process consisted of 0.5 s TDMAHf followed by a 6-s N_2 purge, followed
84 by 0.5 s O_3, followed by a 9-s N_2 purge. In total, 49 cycles were performed at 350 °C to
85 deposit the 5-nm thick HfO_2 film. Finally, a 100 nm Ti top electrode (TE) was deposited
86 using an e-beam evaporator and, as with the BE pattern, the TE pattern was completed using
87 photolithography and lift-off processes. The DC I-V characteristics of the fabricated devices
88 were recorded using a semiconductor parameter analyzer (SPA; Keithley 4200-SCS). Finally,
89 pulse measurements were conducted on a 4225-PMU ultrafast module. A bias was applied to
90 the Ti, while the Pt bottom electrode was grounded.

91 **Results and discussion**

92 The top-view SEM images of the Ti/HfO_2/Pt array and unit cells are presented in Fig. 1(a)
93 and (b), repectively. The line width of the unit cell is about 100 μm. In addition, a cross-
94 sectional TEM image of the Ti/HfO_2/Pt device is presented in Fig. 1(c), and the elementary
95 distribution is revealed by the EDS results in Fig. 1(d). Notably, the EDS map clearly reveals
96 all the features of the stack. Finally, the depth profiles of these elementary compositions are
97 presented in Fig. 1(e).
98 The filament forming process curves of 30 individual cells, whereby the device is activated
99 from the initial state to the low-resistance state (LRS), are presented in Fig. 2(a). Further, the
100 I-V characteristics of the Ti/HfO_2/Pt device during 100 continuous positive SET and negative
101 RESET processes are presented in Fig. 2(b). For comparison, the inset of Fig. 2(b) shows the

102 I-V characteristics obtained during 30 *negative* SET and *positive* RESET processes. The
103 latter I-V curves are less stable than the former because a positive forming voltage allows the
104 oxygen ions generated in the HfO_2 layer to move towards the Ti electrode, thereby creating
105 the TiO_x layer. This TiO_x layer acts as a storage site for the oxygen ions, thus helping to
106 improve the endurance and variability [1]. Subsequently, when a negative voltage is applied
107 during the RESET process, oxygen ions are released from the TiO_x layer and recombine with
108 the oxygen vacancies to change the LRS into a high-resistance state (HRS). By contrast,
109 when a negative forming voltage is applied, the oxygen ions generated in the HfO_2 layer
110 move toward the Pt electrode. Moreover, since Pt is an inert metal that does not readily react
111 with the oxygen ions [1,52], a storage layer is not formed.
112 According to Fig. 2(b), the measured I-V curves do not repeat each other but randomly varied
113 from cycle to cycle demonstrating the stochasticity of the device. As shown in Fig. 2(c), the
114 average values of the positive forming and set voltages are 1.79 V and 1.44 V, respectively.
115 The inset of Figure 2(c) shows the distribution of the SET and forming voltages as a box
116 chart, clearly indicating that the range of SET voltages is wider than the range of forming
117 voltages. The RESET process for multilevel states is shown in Fig. 2(d), wherein the RESET
118 stop voltage is increased from –1.2 V to –2.3 V in steps of 0.1 V. Here, the resistance is seen
119 to change gradually and continuously with each step. This gradual resistance change is
120 suitable for multilevel states in neuromorphic device applications [37]. Further, the pulse
121 endurance during the positive SET and negative RESET process is shown in Fig. 2(e). Here
122 the SET pulse width and voltage amplitude are 500 μs and 1.35 V, respectively, while the
123 RESET pulse width and voltage amplitude are 750 μs and –2.3 V. The conductance values in
124 the HRS and LRS were extracted at a read voltage of 0.2 V. Stable changes in the HRS and
125 LRS are maintained during the first 300 cycles, but become unstable thereafter. At that stage,
126 the SET precess does not proceed properly and the device remains close to the HRS.

127 The DC I-V curves obtained after the 10,000-pulse endurance measurements are presented in
128 Fig. 3(a), while the on/off ratios obtained before and after the endurance test are presented in
129 Fig. 3(b). Here, the on/off ratio is seen to decrease from 1290 before the 10,000 cycles, to 38
130 afterwards. Further, the retention obtained from the initial I-V curve is compared with that
131 obtained after the pulse endurance test in Fig. 3(c). Here, the LRS and HRS conductance
132 states measured before the pulse endurance test are well maintained for 10,000 s whereas,
133 after the pulse endurance test, the LRS is maintained for up to 3,000 s before returning to the
134 HRS with decreasing current. We believe that TiO_x layers were generated at the Ti/HfO_2
135 interface by the multiple pulse stresses. As the dielectric constant of the TiO_x layer (i.e., 33)
136 is larger than that of the HfO_2 (i.e., 25) [22,53], a larger electric field is applied to the HfO_2.
137 This large electric field breaks many Hf–O bonds, thus resulting in more oxygen vacances
138 and oxygen ions in the HfO_2 layer than in the TiO_x layer [22]. For this reason, the amount of
139 oxygen vacancies at the Ti/HfO_2 interface is reduced compared to the initial state, thus
140 resulting in a decreased retention. Further research is needed to confirm this switching
141 mechanism.

142 The stochastic pulse response of the Ti/HfO_2/Pt device is investigated in Fig. 4. First, the SET
143 process by applying a positive pulse voltage is shown in Fig. 4(a). Here, a rapid current
144 change is confirmed by applying read voltages of 0.2 V before and after a 2-ms SET pulse of
145 1.5 V. This result confirms the abrupt SET process seen in the I-V curves of Fig. 2b. Further,
146 an increase in the current value of the read voltage was confirmed after application of the
147 pulse voltage. In a similar manner, the RESET process by application of a negative pulse
148 voltage is shown in Fig. 4(b). Here, the read voltage obtained before and after application of a
149 2-ms pulse voltage of –2.2 V confirms the gradual decrease in current. As shown in Fig. 2b,
150 the reset current is larger than the compliance current (CC), so the overshoot phenomenon is

151 manifested in the DC sweep and pulse process. The rectangular pulse voltage (V_P) can be
152 used to investigate the statistical properties of switching processes. The microscopic
153 mechanisms of switching processes in the Ti/HfO_2/Pt device are shown schematically in Fig.
154 5. Here, Fig. 5(a) represents the initial state before the forming process. For the forming step,
155 a positive voltage is applied so that oxygen ions are generated in the HfO_2 layer and drift
156 towards the Ti electrode (Fig. 5(b)). Then, as shown in Fig. 5(c), the oxygen-ion storing TiO_x
157 layer is formed, along with a conductive filament of oxygen vacancies in the HfO_2 layer for
158 the LRS. Then, when a negative voltage is applied, the TiO_x layer releases the oxygen ions,
159 and the conductive filament is ruptured; i.e., its length is decreased and the RESET process
160 occurs (Fig. 5(d)). The HRS is achieved by completion of the RESET process (Fig. 5(e)),
161 after which the re-application of a positive voltage causes the oxygen ions to move towards
162 the Ti electrode again, and the length of conductive filament grows to its maximal value, thus
163 returning the device to the LRS (Fig. 5(f)). This is essentially a random process and switching
164 times as well as conductance values in HRS and LRS are random values.
165 This stochastic nature of switching processes is clearly visible form the measured
166 characteristics shown in Fig. 2. The switching times can be defined as the first passage times
167 (FPT) of random process $I(t)$ to reach some threshold value. In the present paper, the
168 relationship between the FPT (t_{SET}) and V_P is investigated. In Fig. 4(c), the t_{SET} values are
169 defined as the time of random process $I(t)$ to reach the threshold value 1mA. The amplitude
170 of rectangular pulse V_P was varied from 1.6 V to 1.9 V in steps of 0.1 V. In average the t_{SET}
171 becomes shorter as the V_P increases, thus indicating that t_{SET} is closely related to both the
172 speed of movement of oxygen ions and the V_P. In other words, increasing the V_P increases

173 both the speed of movement of oxygen ions and the switching time to LRS. The mean FPT
174 (MFPT) values of t_{SET} averaged over 10 measurements for each V_P level are shown as black
175 dots in Fig. 4(d) in semilog scale.
176 For analysis of these data we can consider a simple stochastic model of memristor proposed
177 in Ref. [51], where the length of conductive filament is used as the state variable y. In
178 general the value y can be varied in the interval from 0 to L where $L = 5$ nm is the thickness
179 of HfO_2 switching layer. After the forming process the value y is switched between y_{HRS} and
180 y_{LRS} which are random values. The variability of y_{HRS} and y_{LRS} reflects the distribution of
181 conductance in HRS and LRS shown in Fig.2e since the length y is involved in nonlinear
182 Ohmic dependence $I(V, y)$. There are various expressions for it in the literature, for example
183 according to Ref. [54] we have the following

184 $$I(V, y) = \left(\frac{y}{L}\right)^n c_1 \sinh c_2 V + c_3 (e^{c_4 V} - 1), \quad (1)$$

185 where n and c_i are fitting constants. In the simplest case the stochastic equation for the state
186 varable y reads [51]

187 $$\frac{dy}{dt} = v_{eff} + \xi(t), \quad (2)$$

188 where $\xi(t)$ is the white Gaussian noise with $< \xi(t) >= 0$, $< \xi(t)\xi(t+\tau) >= 2D_{eff}\delta(\tau)$, $\delta(\tau)$ is
189 delta function and the value $2D_{eff}$ is the noise intensity. D_{eff} and v_{eff} are the effective
190 diffusion and drift coefficients with the following expressions

191 $$D_{eff} = \frac{\ell^2}{\tau_{kr}} \cosh \alpha(V), \quad (3a)$$

192 $$v_{eff} = \frac{2\ell}{\tau_{kr}} \sinh \alpha(V), \quad (3b)$$

193 where ℓ is effective distance of the vacancies hopping between potential wells separated by

194 potential barriers with the height equal to the activation energy E_a in the microstructure of

195 dielectric material, and τ_{kr} is the Kramers time

196 $$\tau_{kr} = \tau_0 e^{\beta}, \quad (4)$$

197 where $\beta = E_a / k_B T$, T is the temperature, k_B is the Botzmann constant. The prefactor τ_0 is

198 defined by the shape of the potential barriers and wells. The $\alpha(V)$ parameter of Eqs. (3) is

199 given by

200 $$\alpha(V) = \frac{BV}{k_B T}, \quad (5)$$

201 where B is a fitting constant which can be different for positive and negative voltage.

202 Solving numerically the equation (2) we should take into account the reflective boundaries

203 for variable y at $y = 0$ and $y = L$, so y always remains in the interval $[0, L]$. The above

204 model provides a theoretical estimation for the MFPT t_{SET}. For simplicity, we can consider

205 $y_{HRS} = L/2$ and $y_{LRS} = L$. Then, according to [51], if $\beta \gg 1$ and $\alpha \gg 1$ the MFPT of the

206 system variable starting from HRS to reach LRS is

207 $$t_{SET} = \frac{\tau_0}{2} \frac{L}{\ell} \exp(\beta - \alpha(V)). \quad (6)$$

208 Taking into account Eq. (5) the dependence of $\lg t_{SET}(V)$ should be linear as it appears in

209 Fig. 4(d)

210 $$\lg t_{SET} = a - kV, \quad (7)$$

211 where $a = \lg \frac{\tau_0}{2}\frac{L}{\ell} + \frac{E_a}{k_B T}\lg e$ and $k = \frac{B}{k_B T}\lg e$. Both parameters can be estimated from the
212 experimental plot in Fig. 4(d). Assuming $T = 300$ K, $L/\ell = 20$, $\tau_0 = 10^{-9}$ s we obtain
213 $E_a = 1.3$ eV and $B = 0.6$ eV/V. The obtained value of activation energy is in agreement with
214 the estimations and measurements performed in other papers [25,55]. According to Ref. [25]
215 the activation energy for defect migration has a uniform distribution between 0.7 and 1.7 eV
216 with the average value of 1.2 eV. The measurement of the retention time under different
217 temperatures performed in Ref. [55] provides $E_a = 1.55$ eV. The coefficient B shows how
218 much the energy barrier E_a is lowered under the action of the driving voltage. For example,
219 when we change the driving voltage from $V = 0$ up to $V_p = 1.9$ V the dimensionless
220 (normalized to $k_B T$) energy barrier for defects migration is reduced from 52 down to 6. It
221 leads to a very fast growth of conductive filament length and abrupt transition to LRS. On the
222 other hand, if we consider the value of activation energy $E_a = 1.55$ eV independently
223 measured in Ref. [55] as initial parameter, then from the measured data of t_{SET} we can
224 estimate the working temperature of internal area of switching layer, obtaining $T = 348$ K.
225 A thin gap between the conductive filament and TE suggest that the tunneling mechanism of
226 conductivity might be feasible for the studied 5-nm thick HfO_2 switching layer. To comply
227 with the tunneling process, the resistance should not be highly sensitive to temperature
228 changes. However, the results in Fig. 6(a) indicate that the resistance is significantly changed
229 when the temperature is increased from 313 K to 463 K. Further, the I-V curve is well fitted
230 to the $\ln(I) - V^{1/2}$ for Schottky emission (Fig. 6(b)). The Schottky emission is then obtained
231 by Eq. (1) as

232 $$J = A^{*}T^{2}\exp\left[\frac{-q(\varphi_B - \sqrt{qE/4\pi\varepsilon})}{KT}\right] \quad \textbf{(8)}$$

233 where A^* is the effective Richarson constant, q is the magnitude of the electronic charge,

234 φ_B is the barrier height, ε is the high frequency relative dielectric constant, T is the absolute

235 temperature, and K is the Boltzmann constant [34,56]. The intercept and the slope obtained

236 from $\ln(I) - V^{1/2}$ can be expressed as

237 $$|intercept| \propto \varphi_B \quad \textbf{(9a)}$$

238 $$Slope \propto \sqrt{\frac{1}{\varepsilon_i d}} \quad . \quad \textbf{(9b)}$$

239 Schottky emission occurs when thermally activated electrons are injected over the energy

240 barrier into the conduction band of the oxide. This is one of the most often observed

241 conduction mechanisms in metal oxide films [57].

242 Finally, the multilevel characteristics of the Ti/HfO_2/Pt devices are demonstrated in Fig. 7 by

243 emulating the LTP and LTD characteristics of the synapse. In Fig. 7(a), the conductance is

244 modulated by the application of various voltages with an identical pulse width, and obtained

245 at a read voltage of 0.2 V. Here, potentiation is obtained by increasing the pulse voltages

246 from 1.1 V to 1.7 V in steps of 0.2 V at the fixed pulse width of 250 μs, while depression is

247 obtained by decreasing the pulse voltage from –1.1 V to –1.7 V in steps of –0.2 V at a fixed

248 pulse width of 800 μs. The SET pulse width is chosen to be smaller than the RESET pulse

249 width because the SET process is conducted more abruptly. With the identical pulse width,

250 when the magnitude of the voltage is large, a large conductance change is induced by the first

251 pulse. This has the disadvantage that the linearity of the conductance update becomes poor.

252 As shown in Fig. 7(b), the incremental pulse voltage method can be used to obtain a more

253 linear conductance update. Here, the conductance is seen to increase as the pulse input

254 voltage is increased from 1.28 V to 1.55 V in steps of 0.3 V, with 5 pulses being applied for

255 each voltage value. Similarly, the conductance decreases as the pulse input voltage is
256 decreased from –1.2 V to –1.47 V in steps of –0.03 V, with 5 pulses being applied for each
257 voltage value. These results demonstrate that the increamental pulse amplitude method is
258 effective for changing the conductance value, and is more effective than the identical pulse
259 amplitude method for obtaining a linear conductance update. Further, the spike-timing
260 dependent plasticity (STDP) characteristics of the Ti/HfO_2/Pt device, whereby the
261 conductance change depends on the interval between the pre-spike and the post-spike, are
262 indicated in Fig. 7(c). As shown in the inset, the pre- and post-spikes were applied at
263 increasing voltages in the order of 1.3 V, 0.5 V, 0.4 V, 0.3 V, 0.2 V, and 0.1 V. As for the I-V
264 characteristics, a gradual conductance modulation in the LTD (RESET) was measured,
265 whereas the LTP (SET) exhibited little change in conductance once the interval between the
266 pre-spike and post-spike reached 4 ms. Here, the threshold SET voltage is seen to be 1.5 V.

267 **4. Conclusions**

268 In this study, the non-volatile memory characteristics of a Ti/HfO_2/Pt device with a crossbar
269 array structure have been investigated. Due to the asymmetric work function of the metal
270 electrodes, the current-voltage (I-V) characteristics depends on the forming polarity. After a
271 positive forming process, multilevel states and 10,000 pulse endurance cycles have been
272 measured. The retention time is shown to be reduced after pulse endurance cycling. In
273 addition, the voltage-induced switching speed is measured by applying a pulse voltage during
274 the SET process and described using a stochastic model of memristor based on the length of
275 conductive filament. The estimation of dielectric switching layer parameters such as
276 activation energy of diffusing defects, its variation under the influence of driving voltage and
277 value of working temperature havs been obtained through the statistical properties of the
278 MFPT. To analyze the conduction mechanism, the high resistance state (HRS) value has been

279 measured by varying the ambient temperature, and fitted according to the formula for the
280 Schottky emission conduction mechanism. The potentiation and depression have been
281 measured, and spike-time dependent plasticity (STDP) curves have been plotted in order to
282 mimic the characteristics of synapses. The threshold voltage in the abrupt SET process has
283 been determined from the STDP curve. We finally note that the observed gradual change in
284 conductance is suitable for a synaptic device in a neuromorphic system.

285 **Funding**

286 This work was supported in part by a National Research Foundation of Korea (NRF) grant funded by Ministry
287 of Science and ICT (2021R1C1C1004422) and by Government of the Russian Federation through Agreement
288 No. 074-02-2018-330 (2).

289 **References**

290 [1] L. Wu, H. Liu, J. Lin, S. Wang, Volatile and Nonvolatile Memory Operations
291 Implemented in a Pt/HfO2/Ti Memristor, IEEE Trans. Electron Devices. 68 (2021)
292 1622-1626.
293 [2] A. Sawa, Resistive switching in transition metal oxides, Mater. Today. 11 (2008) 28-
294 36.
295 [3] M.K. Rahmani, M.H. Kim, F. Hussain, Y. Abbas, M. Ismail, K. Hong, C. Mahata, C.
296 Choi, B.G. Park, S. Kim, Memristive and synaptic characteristics of nitride-based
297 heterostructures on si substrate, Nanomaterials. 10 (2020) 994.
298 [4] J. Woo, K. Moon, J. Song, S. Lee, M. Kwak, J. Park, H. Hwang, Improved synaptic
299 behavior under identical pulses using AlOx/HfO2 bilayer RRAM array for
300 neuromorphic systems, IEEE Electron Device Lett. 37 (2016) 994-997.
301 [5] J. Won Seo, S.J. Baik, S.J. Kang, Y.H. Hong, J.H. Yang, K.S. Lim, A ZnO cross-bar
302 array resistive random access memory stacked with heterostructure diodes for
303 eliminating the sneak current effect, Appl. Phys. Lett. 98 (2011) 233505
304 [6] Y. LeCun, Y. Bengio, G. Hinton, Deep learning, Nature. 521 (2015) 436-444.
305 [7] I. Boybat, M. Le Gallo, S.R. Nandakumar, T. Moraitis, T. Parnell, T. Tuma, B.
306 Rajendran, Y. Leblebici, A. Sebastian, E. Eleftheriou, Neuromorphic computing with
307 multi-memristive synapses, Nature Comm. 9 (2018) 2514.
308 [8] Y. Li, Z. Wang, R. Midya, Q. Xia, J.J. Yang, Review of memristor devices in
309 neuromorphic computing: materials sciences and device challenges, J. Phys. D: Appl.
310 Phys. 51 (2018) 503002.
311 [9] D.B. Strukov, G.S. Snider, D.R. Stewart, R.S. Williams, The missing memristor fo
312 und, Nature 453 (2008) 80–83.
313 [10] T. Guo, K. Pan, Y. Jiao, B. Sun, C. Du, J.P. Mills, Z. Chen, X. Zhao, L. Wei, Y.
314 N. Zhou, Y.A. Wu, Versatile memristor for memory and neuromorphic computing,
315 Nanoscale Horiz. 7 (2022) 299-310.

316 [11] S. Pi, C. Li, H. Jiang, W. Xia, H. Xin, J.J. Yang, Q. Xia, Memristor crossbar arrays
317 with 6-nm half-pitch and 2-nm critical dimension, Nature Nanotech. 14 (2019) 35–39.
318 [12] Y. Wang, Y. Gong, L. Yang, Z. Xiong, Z. Lv, X. Xing, Y. Zhou, B. Zhang, C. Su, Q.
319 Liao, S. T. Han, MXene-ZnO Memristor for Multimodal In-Sensor Computing, Adv.
320 Funct. Mater. 31 (2021) 2100144.
321 [13] W. Wang, M. Wang, E. Ambrosi, A. Bricalli, M. Laudato, Z. Sun, X. Chen, D. Ielmini,
322 Surface diffusion-limited lifetime of silver and copper nanofilaments in resistive
323 switching devices, Nature Comm. 10 (2019) 81.
324 [14] Y. Wang, Y. Gong, S. Huang, X. Xing, Z. Lv, J. Wang, J.Q. Yang, G. Zhang, Y. Zhou,
325 S.T. Han, Memristor-based biomimetic compound eye for real-time collision detection,
326 Nature Comm. 12 (2021) 5979.
327 [15] Z. Lv, Y. Zhou, S.T. Han, V.A.L. Roy, From biomaterial-based data storage to bio-
328 inspired artificial synapse, Mater. Today 21 (2018) 537-552.
329 [16] C. Mahata, C. Lee, Y. An, M.H. Kim, S. Bang, C.S. Kim, J.H. Ryu, S. Kim, H. Kim,
330 B.G. Park, Resistive switching and synaptic behaviors of an HfO2/Al2O3 stack on
331 ITO for neuromo-phic systems, J. Alloy. Compd. 826 (2020) 154434.
332 [17] H. Wang, L. Hu, W. Han, Resistive switching behavior, mechanism and synaptic
333 characteristics in TiO2 nanosheets grown on Ti plate by hydrothermal method, 854
334 (2021) 157200.
335 [18] Z. Lv, Y. Wang, J. Chen, J. Wang, Y. Zhou, S.-T. Han, Semiconductor Quantum Dots
336 for Memories and Neuromorphic Computing Systems, Chem. Rev. 120 (2020)
337 3941−4006.
338 [19] W. Huang, X. Xia, C. Zhu, P. Steichen, W. Quan, W. Mao, J. Yang, L. Chu, X. Li,
339 Memristive Artifcial Synapses for Neuromorphic Computing, Nano-Micro Lett. 13
340 (2021) 85.
341 [20] S. Yu, H.Y. Chen, B. Gao, J. Kang, H.S.P. Wong, HfOx-based vertical resistive
342 switching random access memory suitable for bit-cost-effective three-dimensional
343 cross-point architecture, ACS Nano. 7 (2013) 2320-2325.
344 [21] C.H. Cheng, A. Chin, F.S. Yeh, Stacked GeO/ SrTiOx resistive memory with ultralow
345 resistance currents, Appl. Phys. Lett. 98 (2011) 052905.
346 [22] M. Ismail, U. Chand, C. Mahata, J. Nebhen, S. Kim, Demonstration of synaptic and
347 resistive switching characteristics in W/TiO2/HfO2/TaN memristor crossbar array for
348 bioinspired neuromorphic computing, J. Mater. Sci. Technol. 96 (2022) 94-102.
349 [23] M. Ismail, C. Mahata, S. Kim, Forming-free Pt/Al2O3/HfO2/HfAlOx/TiN memristor
350 with controllable multilevel resistive switching and neuromorphic characteristics for
351 artificial synapse, J. Alloy. Compd. 892 (2022) 162141.
352 [24] K.L. Lin, T.H. Hou, J. Shieh, J.H. Lin, C.T. Chou, Y.J. Lee, Electrode dependence of
353 filament formation in HfO2 resistive-switching memory, J. Appl. Phys. 109 (2011)
354 084104.
355 [25] S. Ambrogio, S. Balatti, A. Cubeta, A. Calderoni, N. Ramaswamy, D. Ielmini,
356 Statistical fluctuations in HfOx resistive-switching memory: Part I-Set/Reset
357 variability, IEEE Trans. Electron Devices. 61 (2014) 2912-2919.
358 [26] Z. Yan, Y. Guo, G. Zhang, J.M. Liu, High-performance programmable memory
359 devices based on Co-doped $BaTiO_3$, Adv. Mater. 23 (2011) 1351-1355.
360 [27] J. Choi, S. Kim, Coexistence of Long-Term Memory and Short-Term Memory in an
361 SiNx-Based Memristor, Phys. Status Solidi-Rapid Res. Lett. 14 (2020) 2000357.
362 [28] S. Kim, Y.F. Chang, B.G. Park, Understanding rectifying and nonlinear bipolar
363 resistive switching characteristics in Ni/SiNx/p-Si memory devices, RSC Adv. 7
364 (2017) 17882-17888.

365 [29] S. Kim, S. Cho, K.-C. Ryoo, B.-G. Park, Effects of conducting defects on resistive
366 switching characteristics of SiNx-based resistive random-access memory with MIS
367 structure, J. Vac. Sci. Technol B. 33 (2015) 062201.
368 [30] H.D. Kim, M. Yun, S. Kim, Self-rectifying resistive switching behavior observed in
369 Si3N4-based resistive random access memory devices, J. Alloy. Compd. 651 (2015)
370 340-343.
371 [31] B. Kim, H.S. Choi, Y. Kim, A study of conductance update method for Ni/SiNx/Si
372 analog synaptic device, Solid-State Electron. 171 (2020) 107772.
373 [32] J.H. Ryu, B. Kim, F. Hussain, M. Ismail, C. Mahata, T. Oh, M. Imran, K.K. Min, T.H.
374 Kim, B. do Yang, S. Cho, B.G. Park, Y. Kim, S. Kim, Zinc Tin Oxide Synaptic Device
375 for Neuromorphic Engineering, IEEE Access. 8 (2020) 130678-130686.
376 [33] J. Lee, J.H. Ryu, B. Kim, F. Hussain, C. Mahata, E. Sim, M. Ismail, Y. Abbas, H.
377 Abbas, D.K. Lee, M.H. Kim, Y. Kim, C. Choi, B.G. Park, S. Kim, Synaptic
378 Characteristics of Amorphous Boron Nitride-Based Memristors on a Highly Doped
379 Silicon Substrate for Neuromorphic Engineering, ACS Appl. Mater. Interfaces. 12
380 (2020) 33908-33916.
381 [34] L. Zhang, Z. Xu, J. Han, L. Liu, C. Ye, Y. Zhou, W. Xiong, Y. Liu, G. He, Resistive
382 switching performance improvement of InGaZnO-based memory device by nitrogen
383 plasma treatment, J. Mater. Sci. Technol. 49 (2020) 1-6.
384 [35] X.A. Tran, W.G. Zhu, B. Gao, J.F. Kang, W.J. Liu, Z. Fang, Z.R. Wang, Y.C. Yeo,
385 B.Y. Nguyen, M.F. Li, H.Y. Yu, A self-rectifying HfOx-based unipolar RRAM with
386 NiSi electrode, IEEE Electron Device Lett. 33 (2012) 585-587.
387 [36] J. Niu, M. Zhang, Y. Li, S. Long, H. Lv, Q. Liu, M. Liu, Highly scalable resistive
388 switching memory in metal nanowire crossbar arrays fabricated by electron beam
389 lithography, J. Vac. Sci. Technol B. 34 (2016).
390 [37] S. Kim, H. Kim, S. Hwang, M.H. Kim, Y.F. Chang, B.G. Park, Analog Synaptic
391 Behavior of a Silicon Nitride Memristor, ACS Appl. Mater. Interfaces. 9 (2017)
392 40420-40427.
393 [38] J. Joshua Yang, F. Miao, M.D. Pickett, D.A.A. Ohlberg, D.R. Stewart, C.N. Lau, R.S.
394 Williams, The mechanism of electroforming of metal oxide memristive switches,
395 Nanotechnology. 20 (2009) 215201.
396 [39] Y. Li, K.S. Yin, M.Y. Zhang, L. Cheng, K. Lu, S.B. Long, Y. Zhou, Z. Wang, K.H.
397 Xue, M. Liu, X.S. Miao, Correlation analysis between the current fluctuation
398 characteristics and the conductive filament morphology of HfO2-based memristor,
399 Appl. Phys. Lett. 111 (2017) 213505.
400 [40] C. Guarcello, D. Valenti, B. Spagnolo, Phase dynamics in graphene-based Josephson
401 junctions in the presence of thermal and correlated fluctuations, Phys. Rev. B 92
402 (2015) 174519.
403 [41] A. Caruso, M. E. Gargano, D. Valenti, A. Fiasconaro, B. Spagnolo, Cyclic
404 Fluctuations, Climatic Changes and Role of Noise in Planktonic Foraminifera in The
405 Mediterranean Sea, Fluct. Noise Lett. 5 (2005) L349-L355.
406 [42] C. Guarcello, D. Valenti, B. Spagnolo, V. Pierro, G. Filatrella, Anomalous Transport
407 Effects on Switching Currents of Graphene-based Josephson junctions,
408 Nanotechnology 28 (2017) 134001.
409 [43] A. Carollo, D. Valenti, B. Spagnolo, Geometry of quantum phase transitions, Physics
410 Reports 838 (2020) 1-72.
411 [44] C. Guarcello, D. Valenti, A. Carollo and B. Spagnolo, Stabilization Effects of
412 Dichotomous Noise on the Lifetime of the Superconducting State in a Long Josephson
413 Junction, Entropy 17 (2015) 2862-2875.

414 [45] A.V. Yakimov, D.O. Filatov, O.N. Gorshkov, D.A. Antonov, D.A. Liskin, I.N.
415 Antonov, A.V. Belyakov, A.V. Klyuev, A. Carollo, B. Spagnolo, Measurement of the
416 activation energies of oxygen ion diffusion in yttria stabilized zirconia by flicker noise
417 spectroscopy, Appl. Phys. Lett. 114 (2019) 253506.
418 [46] Y.V. Ushakov, A.A. Dubkov, B. Spagnolo, Spike train statistics for consonant and
419 dissonant musical accords in a simple auditory sensory model, Phys. Rev. E 81 (2010)
420 041911.
421 [47] D.O. Filatov, D.V. Vrzheshch, O.V. Tabakov, A.S. Novikov, A.I. Belov, I.N.
422 Antonov, V.V. Sharkov, M.N. Koryazhkina, A.N. Mikhaylov, O.N. Gorshkov, A.A.
423 Dubkov, A. Carollo, B. Spagnolo, Noise-induced resistive switching in a memristor
424 based on ZrO2(Y)/Ta2O5 stack, J. Stat. Mech-Theory Exp. 2019 (2019) 124026.
425 [48] B. Lisowski, D. Valenti, B. Spagnolo, M. Bier, E. Gudowska-Nowak, Stepping
426 molecular motor amid Lévy white noise, Phys. Rev. E 91 (2015) 042713.
427 [49] A. Carollo, B. Spagnolo, A.A. Dubkov, D. Valenti, On quantumness in multi-
428 parameter quantum estimation, J. Stat. Mech-Theory Exp. 2019 (2019) 094010.
429 [50] N.V. Agudov, A.V. Safonov, A.V. Krichigin, A.A. Kharcheva, A.A. Dubkov, D.
430 Valenti, A.N. Mikhailov, A. Carollo, B. Spagnolo, Nonstationary distributions and
431 relaxation times in a stochastic model of memristor, J. Stat. Mech-Theory Exp. 2020
432 (2020) 024003.
433 [51] N.V. Agudov, A.V. Safonov, A.V. Krichigin, A.A. Kharcheva, A.A. Dubkov, D.V.
434 Guseinov, M.A. Koriazhkina, A.S. Novikov, V.A. Shishmakova, I.N. Antonov, A.
435 Carollo, B. Spagnolo, Stochastic model of memristor based on conductive filament
436 length, Chaos Soliton Fract. 150 (2021) 111131.
437 [52] R. Schmiedl, V. Demuth, P. Lahnor, H. Godehardt, Y. Bodschwinna, C. Harder, L.
438 Hammer, H.P. Strunk, M. Schulz, K. Heinz, Oxygen diffusion through thin Pt films on
439 Si(100), Appl. Phys. A-Mater. Sci. Processing. 62 (1996) 223-230.
440 [53] V. Fiorentini, G. Gulleri, Theoretical evaluation of zirconia and hafnia as gate oxides
441 for Si microelectronics, Phys. Rev. Lett. 89 (2002) 266101.
442 [54] J.J. Yang, M.D. Pickett, X. Li, D.A. Ohlberg, D.R. Stewart, R.S. Williams, Memristive
443 switching mechanism for metal/oxide/metal nanodevices, Nature Nanotech. 3
444 (2008) 429–433.
445 [55] H. Jiang, L. Han, P. Lin, Z. Wang, M.H. Jang, Q. Wu, M. Barnell, J.J. Yang, H.L. Xin,
446 Q. Xia, Sub-10 nm Ta Channel Responsible for Superior Performance of a
447 HfO_2 Memristor, Sci. Rep. 6 (2016) 28525.
448 [56] P.C. Yang, T.C. Chang, S.C. Chen, H.H. Su, J. Lu, H.C. Huang, D.S. Gan, N.J. Ho,
449 Improvement on low-temperature deposited HfO2 film and interfacial layer by high-
450 pressure oxygen treatment, Solid-State Electron. 62 (2011) 128-131.
451 [57] J. Zhu, T. Zhang, Y. Yang, R. Huang, A comprehensive review on emerging artificial
452 neuromorphic devices, Appl. Phys. Rev. 7 (2020) 011312.

453

454

455

456 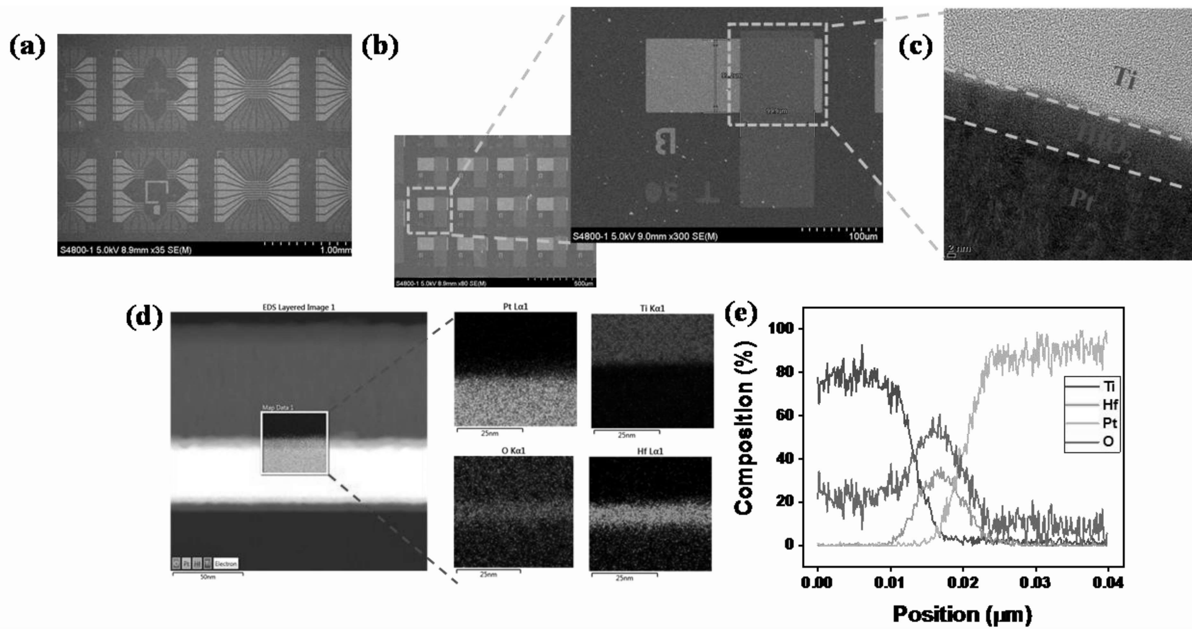

457 Fig. 1 (a and b) The top view SEM images of (a) the crossbar array structure, and (b) a unit

458 cell, of the Ti/HfO_2/Pt device. (c–e) A TEM image (c), EDS color mappings for the elements

459 Pt, Ti, O, and Hf (d), and the corresponding EDS line profile (e), revealing the stacked

460 structure of the Ti/HfO_2/Pt device.

461
462
463
464
465
466
467

468

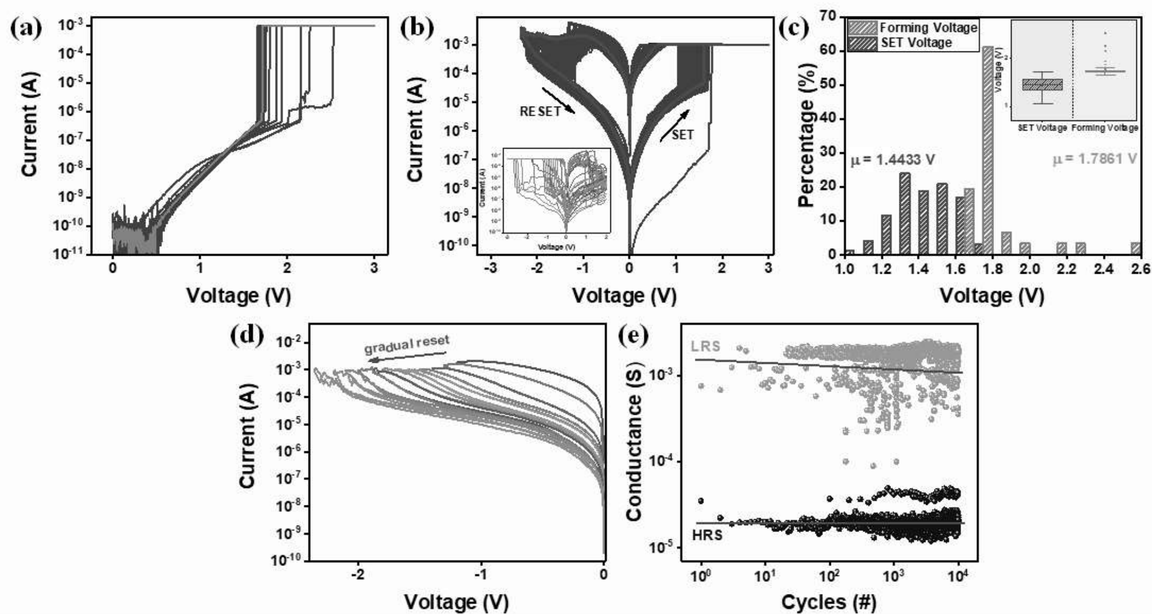

469 Fig. 2 The bipolar resistive switching characteristics of the Ti/HfO_2/Pt device: (a) the forming

470 curves; (b) the I-V characteristics of the positive SET process, with an inset showing the I-V

471 characteristics of the negative SET process; (c) the forming and SET voltage distributions;

472 (d) the RESET transition for multi-level states by increasing the reset stop voltage; and (e)

473 the pulse endurance (10,000 cycles).

474
475
476
477
478
479
480
481
482
483
484
485

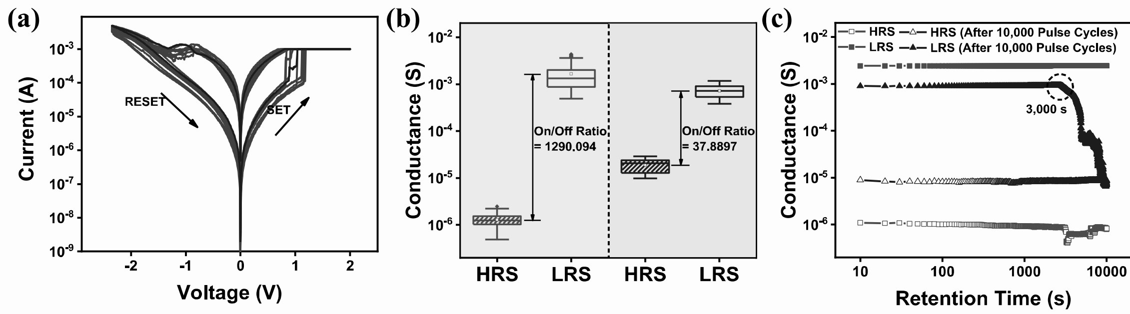

486

487 Fig. 3 (a) The I-V characteristics of the Ti/HfO_2/Pt device after the pulse endurance test. (b and c)

488 Comparison between the pre- and post-endurance I-V characteristics: (b) resistance box chart, and (c)

489 retention characteristics.

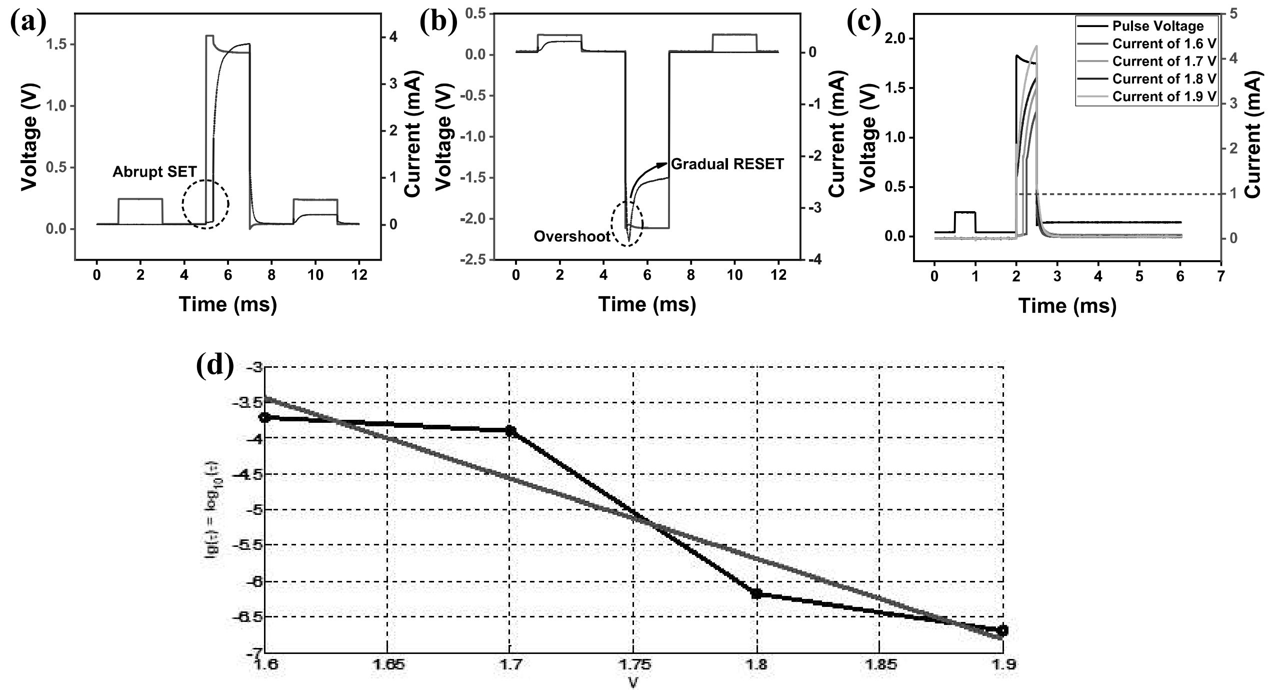

490

491

492 Fig. 4 The pulse response of the Ti/HfO_2/Pt device: (a) the SET process, (b) the RESET process, (c) the FPT

493 (t_{SET}) to reach threshold level 1mA according to pulse voltage (V_P), and (d) Black dots show the MFPT t_{SET} vs

494 pulse aplitude V_p in semilog scale approximated by linear plot (8) with parameters $a = 15.5$ and $k = 11.2$

495

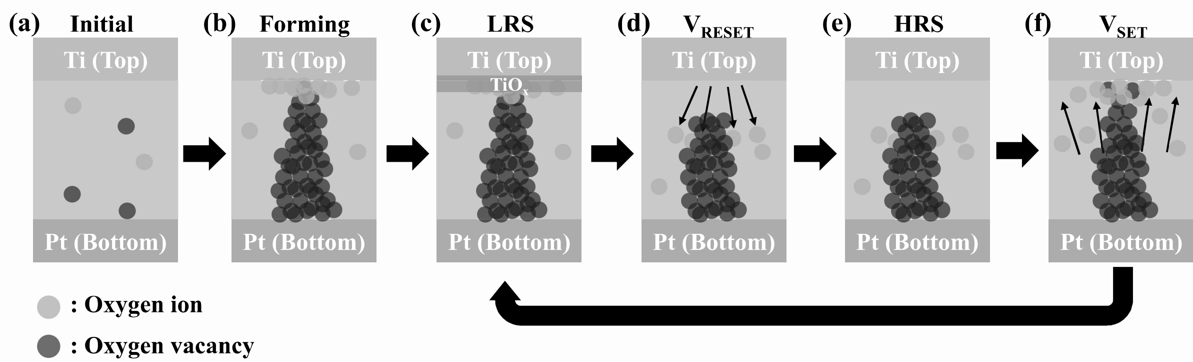

496

497 Fig. 5 Schematic diagrams showing the swithching process in the Ti/HfO_2/Pt device: (a) the initial state, (b) the
498 forming stage, (c) the LRS, (d) application of V_{RESET} , (e) the HRS, (f) application of V_{SET}.

499

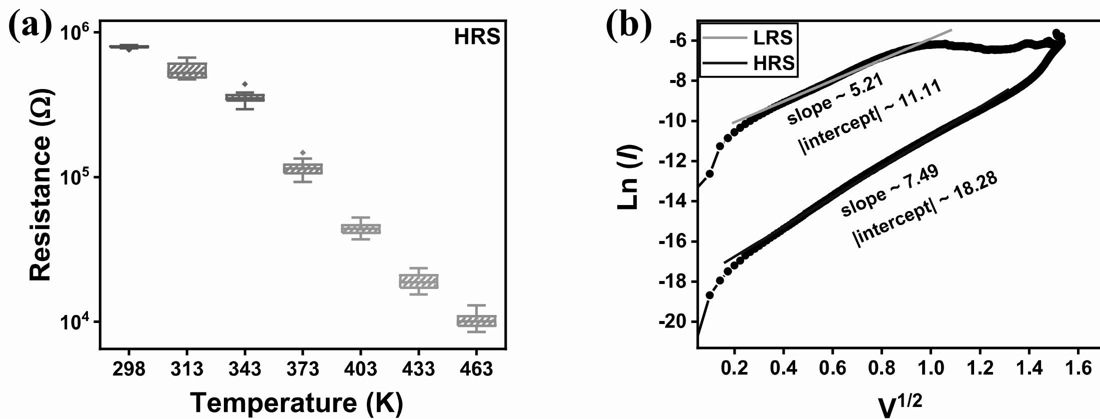

500

501 Fig. 6 (a) The behavior of the resistance versus the temperature in HRS. (b) The plot of ln(I) versus $V^{1/2}$ for
502 Schottky conduction.

503

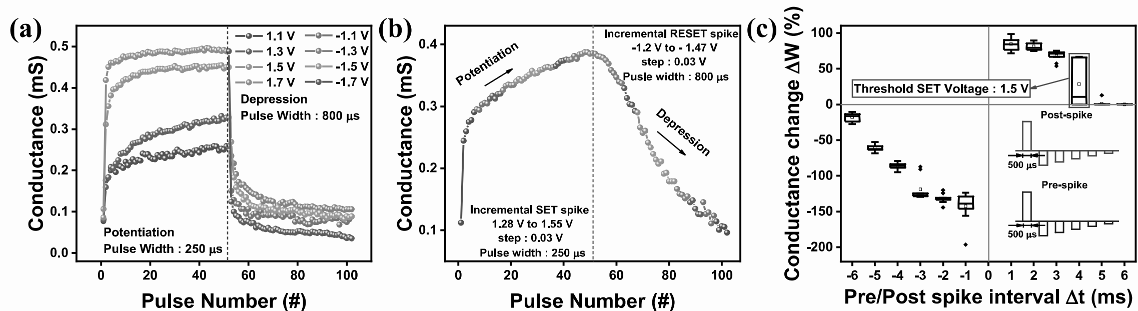

504
505 Fig. 7 The synaptic behavior of the Ti/HfO_2/Pt device: (a) under various pulse voltages with identical pulse
506 width, (b) the incremental pulse response, and (c) the STDP behavior (inset: consecutive pulse trains with
507 different voltage amplitudes).